Cambrian mafic and granitic intrusions in the Mazar-Tianshuihai terrane, West Kunlun Orogenic Belt: Constraints on the subduction orientation of the Proto-Tethys Ocean

Xiao-Qiang Liu [a], Chuan-Lin Zhang [a, *], Xian-Tao Ye [a], Haibo Zou [b, c], Xiao-Shu Hao [a]

[a] College of Oceanography, Hohai University, Nanjing, 210098, China
[b] Department of Geosciences, Auburn University, Auburn, AL, 36849, USA
[c] State Key Laboratory of Continental Dynamics, Department of Geology, Northwest University, Xi'an, 710069, China

ARTICLE INFO

Article history:
Received 13 July 2019
Received in revised form
8 September 2019
Accepted 19 September 2019
Available online 9 October 2019

Keywords:
Cambrian dolerite/gabbro and granite
Age
Geochemistry
Western Kunlun
Proto-Tethys Ocean

ABSTRACT

The West Kunlun Orogenic Belt (WKOB) carries key information about the evolution of the Proto-Tethys Ocean. In order to have a better understanding of the early Paleozoic tectonic evolution of the WKOB and to unravel the process of the Tarim assemblage to Gondwana, we report fi

terranes and the closing process of the Proto-Tethys Ocean, and whether or not the Tarim block assemblaged to the Eastern Gondwana (e.g., Ducea et al., 2003; Jiang et al., 2002, 2008, 2013; Matte et al., 1996; Mattern and Schneider, 2000; Pan, 1990; Pan and Wang, 1994; Wang et al., 2001, 2002; Wang, 2004; Xiao et al., 1998, 2002a, b, 2005; Yang et al., 1996; Yin and Harrison, 2000; Yuan et al., 2002, 2004, 2005; Zhang et al., 2006, 2007). Especially the subduction polarity of the Proto-Tethys Ocean is under debates. Some geologists favored the northward subduction (Wang, 2004; Xiao et al., 2000), and the Paleozoic Kudi-Qimanyute Ophiolite was considered as the remnant of the back-arc basin of the Proto-Tethys Ocean (Wang et al., 2002; Wang, 2004). Another school of idea suggested the southward subduction polarity of the Proto-Tethys Ocean beneath the South Kunlun Terrane (SKT), which led to the amalgamation between the North Kunlun Terrane (NKT) and SKT in early Paleozoic (Jiang et al., 2002; Mattern and Schneider, 2000; Zhang et al., 2018a, b, c, d; Li et al., 2018). In addition to the above north or south subduction orientations, some workers proposed a double-sided subduction of the Proto-Tethys Ocean model (Xiao et al., 2002a).

The models associated with the subduction polarity of Proto-Tethys Ocean were invoked on the following prerequisites: (1) the SKT was a Precambrian micro-continent, therefore the arc-related granites can be formed and (2) the Paleozoic magmatic rocks in the WKOB trend to be younger from north to south and (3) the magmatic rocks in the Tianshuihai Terrane (TSHT) are all emplaced during Mesozoic and no Paleozoic magmatism occurred. Most workers consider that the Kangxiwa Fault, the boundary between the SKT and TSHT, is the suture zone resulted from the closure of a branch of the Paleo-Tethys Ocean (Ducea et al., 2003; Jiang et al., 2013; Rutte et al., 2017), while others claimed that it is either a syn-accretion fault or a post-accretion fault (Xiao et al., 2002a, b, 2005; Wang, 2004). However, our recent works reveal that the main part of the SKT, i.e., the Saitula Group, was a Paleozoic accretionary complex which may be resulted from the southward subduction of the Proto-Tethys Ocean (Zhang et al., 2018c), and the only confirmed Precambrian basements in the WKOB were the Archean Mazar Terrane (MZT, Fig.1a, Zhang et al., 2018a) and the Neoproterozoic TSHT (Fig.1a, Zhang et al., 2018c). More importantly, the Early Paleozoic igneous rocks, including dolerites, gabbros and granites were identified in the confirmed Precambrian basement, i.e., the Mazar Terrane-Tianshuihai Terrane (MZT-TSHT). These newly identified Early Cambrian magmatic rocks in the MZT-TSHT provide new insights for a more reliable reconstruction of the Paleozoic tectono-magmatism evolution history of the WKOB. In this contribution, we report field observations, ages, and geochemistry of the newly identified Early Paleozoic dolerite/gabbro and granitic intrusions in the Archean MZT and central part of the TSHT, in order to constrain the tectonic signature of the NE Pamir and WKOB and to better understand the tectonic evolution of the Proto-Tethys Ocean and assemblage process between the Tarim and Eastern Gondwana.

2. Regional geology and petrography

The WKOB, adjoins the Tarim Basin to the north, the Tibetan Plateau to the south, and the Pamir Plateau to the west, is offset from East Kunlun Orogen and Songpan-Ganzi Terrane by the Altyn sinistral strike-slip fault to the east (Fig. 1a, Gibbons et al., 2015; Yin and Harrison, 2000). Tectonically, the WKOB can be divided into the eastern and western section. The western section, generally known as the Pamir salient, has been subdivided into three tectonic units, i.e., the Northern Pamir, Central Pamir, and Southern Pamir (Robinson et al., 2007, 2012; Schwab et al., 2004). The 1/250000 mappings and our systematic geochronological studies in this area demonstrated that the main part of the NE Pamir (i.e., Tashikorgan Terrane (TSKT) shown in Fig. 1a) was composed of a Cambrian volcanic-sedimentary sequence, locally known as the Bulunkuole Group (BKG), rather than a Triassic accretionary complex (e.g., Robinson et al., 2012). At its southern margin, the BKG thrust onto the newly identified Archean MZT (Fig. 1a, Ji et al., 2011; Zhang et al., 2018b).

The eastern section of the WKOB can be subdivided into three main tectonic units (Fig. 1a), i.e., the NKT, the SKT and the TSHT, by the Paleozoic Kudi-Qimanyute Suture (KQS), Mazar-Kangxiwa Fault (MKF) and Hongshanhu-Qiaoertianshan Suture (HQS), respectively (Mattern and Schneider, 2000; Xiao et al., 2005). The NKT, an uplifted terrane of Tarim Block, composed of a pre-Nanhuanian metamorphosed and deformed basement and unconformably covered by Nanhua-Cambrian carbonate-clastic- tillite sequences (Zhang et al., 2007, 2016). The main part of SKT, i.e., the Saitula Group, was a metamorphosed Cambrian to early Ordovician accretionary wedge and resembles the BKG in rock assemblage, ages, metamorphism grade and deformation features (Fig. 1a, Zhang et al., 2018c, d). Thus, the BKG and the Saitula Group compose a massive early Paleozoic accretionary wedge distributed between the Tarim and the MZT-TSHT (Fig. 1a). The TSHT is widely covered by glacier deposits and knowledge of its geology is highly incomplete due to geographic remoteness (Cui et al., 2006). Some scholars suggested that this terrane is equivalent to the Songpan-Ganzi block of Tibetan Plateau, which collided with SKT during the Early Mesozoic (Xiao et al., 2005; Liu et al., 2015). The Neoproterozoic Tianshuihai Group (youngest detrital zircon age peaks at ~743 Ma, Zhang et al., 2018c), as the only Precambrian sequence of the TSHT, composed of meta-greywacke and limestone and is in fault or unconformable contact with the late Paleozoic to early Mesozoic accretionary wedge (Zhang et al., 2018c). The thick monotonous and partly metamorphosed successions of clastic marine deposits show flysch signatures (Mattern and Schneider, 2000).

The Early Paleozoic and Mesozoic magmatic rocks associated with the evolution of the Proto- and Paleo-Tethys Ocean are widespread in the WKOB. Previous studies mostly focused on the igneous rocks and some key geological units such as the ophiolites along the Xinjiang-Tibet road and the China-Pakistan road due to the difficult accessibility to most areas of the WKOB (e.g., Mattern and Schneider, 2000; Wang et al., 2002, 2017; Yang et al., 1996; Zhang et al., 2004, 2005, 2016; Liu et al., 2015; Jiang et al., 2013). These studies reveal that the Early Paleozoic magmatic rocks in the WKOB are distributed mainly in the SKT and subordinately in the NKT, while the Mesozoic magmatic rocks in the WKOB are emplaced mainly along the southern part of the SKT and the northern martin of the TSHT (Fig. 1a). The Early Paleozoic granitoids were emplaced in the SKT during 510—400 Ma (Jiang et al., 2002, 2008; Zhang et al., 2018a, 2018b). Geochemically, the early Paleozoic granites in SKT can be defined as two distinct phases and types, i.e., the 510—450 Ma I—type granites and the 430-400 Ma high Ba—Sr and A—type granites (Ye et al., 2008; Yuan et al., 2002, 2005). In combination of the ca.440 Ma amphibolite-facies metamorphism of the SKT, the accretion between Tarim and SKT were finished at ca.440 Ma (Zhang et al., 2018c).

The MZT is located at the southeastern margin of the NE Pamir (Fig. 1a), where the Archean basement in the WKOB was identified (Ji et al., 2011; Zhang et al., 2018b). The Neoarchean sequence was intruded by diverse types of intrusions, including the Neoproterozoic trondhjemite-tonalite-granodiorite and Cambrian dolerite-gabbros and Mesozoic granites (Fig. 1b, Zhang et al., 2018b; this study). To the north of this terrane is the Cambrian accretionary wedge (i.e., the BKG, Zhang et al., 2018a) and at its southeastern side, it was intruded by the Mesozoic granites. The dolerite-gabbros are mostly distributed at the southwestern side of the MZT, shown as stocks and dykes in the field. The stocks outcrop as oval in form

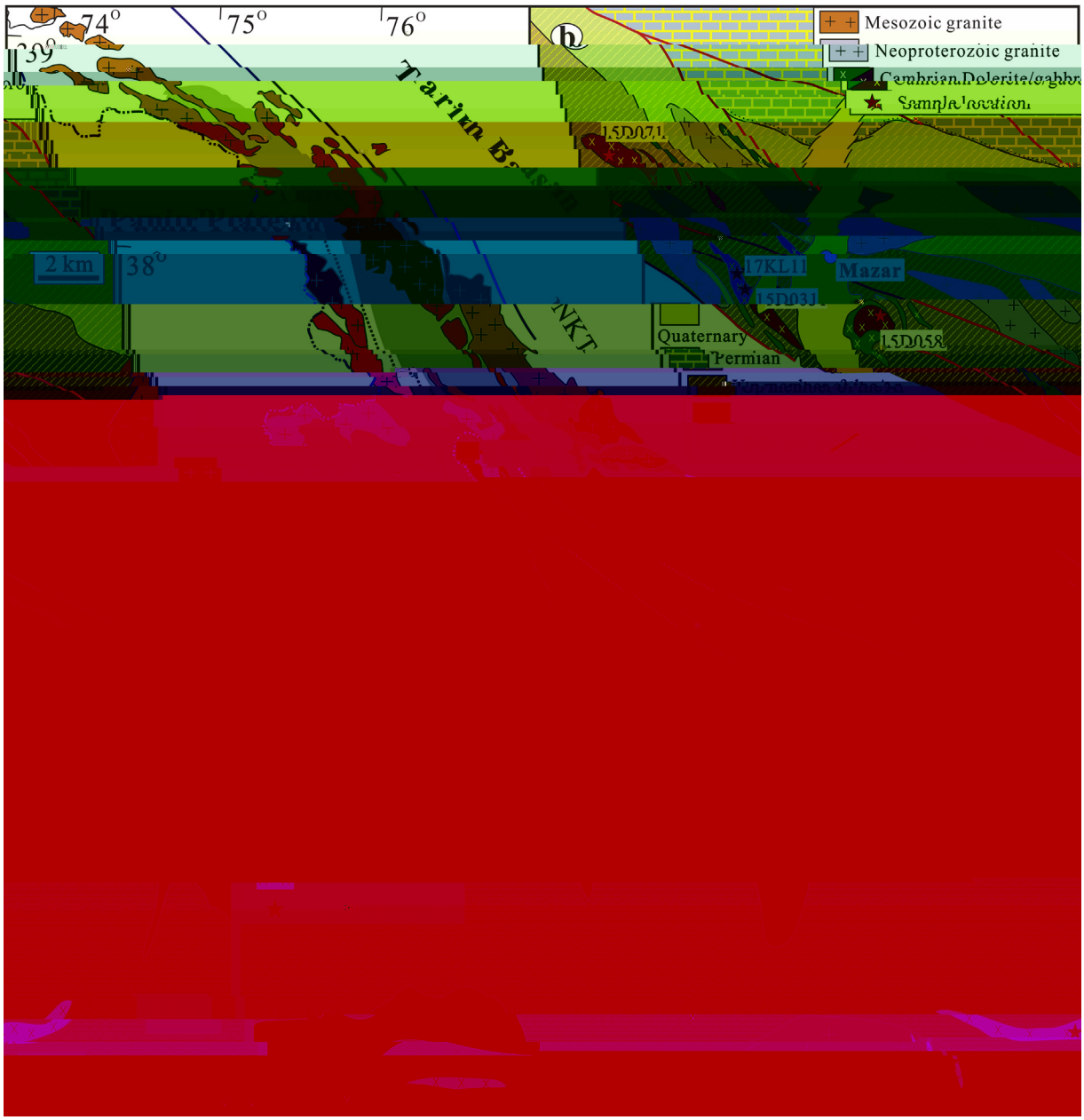

Fig. 1. (a) Simplified tectonic map of the Western Kunlun Orogenic Belt (WKOB), showing the major terranes and related granite plutons (Modified from Zhang et al., 2018d). The so-called basement of TSKT and SKT, locally known as the Bulunkuole Group and Saitula Group, are an early Paleozoic accretionary wedge. NKT—Northern Kunlun terrane; SKT—Southern Kunlun terrane; TSKT—Tashikorgan terrane; TSHT —Tianshuihai terrane; MZT—Mazar Terrane; KQS—Kudi-Qimanyute Suture; MKF—Mazar-Kangxiwa Fault; HQS—Hongshanhu-Qiaoertianshan Suture. (b) Geological map of the Cambrian mafic intrusive rocks in the Mazar terrane. (c) Geological map of the Cambrian magmatic rocks in the Tianshuihai terrane.

with several square kilometers. The dykes mostly strike in NW and are several hundred meters to more than 1 km long and several to hundred meters wide (Fig. 1b).

The TSHT is a NW-SE trending belt, located to the south of Kangxiwa Fault (Fig. 1a). Magmatic rocks in the TSHT were emplaced mainly during Triassic-Jurassic (240-195 Ma) and subordinately during the Early Cambrian (Fig. 1a, Hu et al., 2016 and this study). The Early Cambrian dolerite-gabbros in this contribution are distributed south to the Dahongliutan iron deposit district, central part of the TSHT (Fig. 1c, Hu et al., 2016). The dolerite-gabbros occur as dykes in the field, strike in EW and are hundred meters to several kilometers long and several to dozens of meters wide (Fig. 1c). Zircon LA-ICPMS dating of a gabbro sample near the sample location of this contribution yielded age of 532.3 ± 3.1 Ma (Hu et al., 2016).

The dolerites/gabbros and granites were collected at the MZT (Fig. 1b) and central part of TSHT (Fig. 1c). The dolerite/gabbro samples were altered to variable degrees as identified in the thin sections and the electronic probe analyses (see details in section 4.2), such as replacement of clinopyroxene by hornblende and sericitization of the plagioclase. The gabbro samples consist of pyroxene (all replaced by the hornblende, showing as pyroxene pseudomorph) and plagioclase (Fig. 2a), and consist mainly of brown hornblende (40–60%), sericitized plagioclase (40–50%) and minor Ti–Fe oxide. The dolerites are composed mainly of hornblende (50–65%), sericitized plagioclase (30–50%). The granites are relatively fresh with slight sericitization of the plagioclase (Fig. 2b). They are composed mainly of K-feldspar (50–55%), plagioclase

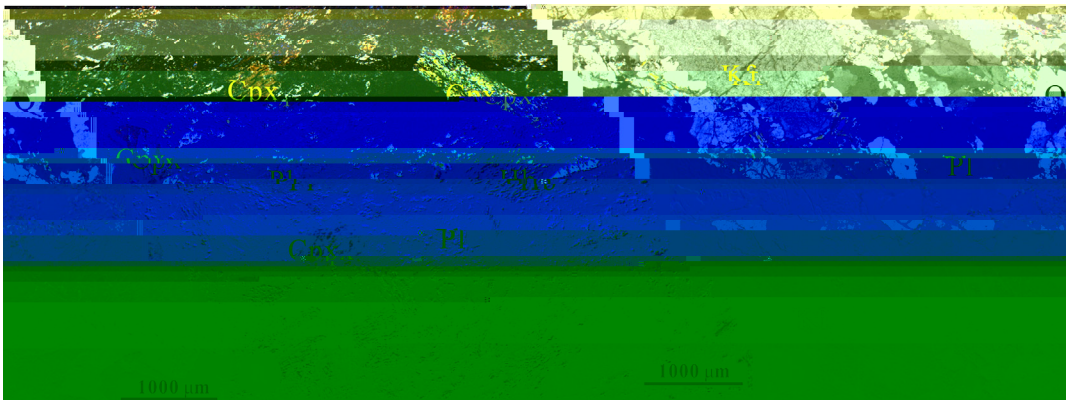

Fig. 2. Microscope photos of the Cambrian mafic (a) and granitic (b) intrusions from the Mazar Terrane-Tianshuihai Terrane. Cpx – Clinopyroxene; Hb – Hornblende; Pl – Plagioclase; Kf – K-feldspar; Q – Quartz; Ser – Sericite.

(10–15%), quartz (30–35%) and minor secondary sericite, with accessory minerals of zircon and apatite.

3. Analytical procedures

Zircon separation was carried out using standard crushing, sieving, and heavy liquid and magnetic separation techniques. Representative zircons were then mounted on a double-sided tape by hand-picking under a binocular microscope. Zircon dating of three samples was carried out at Tianjin Institute of Geology and Mineral Resources (TJIGMR), Chinese Geology Survey (CGS), where a Neptune MC-ICPMS coupled with a 193 nm excimer laser ablation system was used to determine zircon U–Pb ages. The detailed analytical procedures are similar to those of Geng et al. (2011). Zircon dating of a gabbro sample from MZT was conducted on a SHRIMP-II instrument at Beijing SHRIMP Centre (National Science and Technology Infrastructure), using the standard operating conditions (Williams, 1998). Isoplot (Ludwig, 2003) was used for data processing. Zircon U–Pb isotopic data was listed in Tables S1 and S2.

Mineral compositions were determined on thin-sections using an automated JEOL 8800 electron microprobe equipped with 5 wavelength spectrometers at Guangzhou Institute of Geochemistry, Chinese Academy of Sciences. The operating conditions during analyses are 15 keV accelerating voltage and 15 nA beam current with 20 s counting time. The analytical precision is better than 5%. The analytical results of hornblende were listed in Table S3.

Major-element oxides were obtained using Rigaku ZSX100e X-ray fluorescence (XRF) on fused glass beads at the Nanjing Institute of Geology and Mineral Resources (NJIGMR), CGS, following analytical procedures similar to those of Li et al. (2006). Analytical precision was better than 5%. Trace elements were analysed using a PE Elan 600 ICP-MS at the Institute of Geochemistry, Chinese Academy of Science, following procedures similar to those described by Li et al. (2006). In-run analytical precision for most elements was generally better than 2-5%. The analytical results of major and trace elements are listed in Table S4.

Those zircon grains from the MZT mafic rocks are too small to undertake in situ Lu–Hf analyses. Therefore, zircon in situ Lu–Hf isotopic analyses were only conducted on the Cambrian granites in the TSHT. Lu–Hf isotopic compositions of zircons were determined using a Neptune MC-ICPMS at TJIGMR, CAS, following the procedure documented in Geng et al. (2011). The isotopic results are listed in Table S5.

Sr–Nd isotopes were determined using a Micromass Isoprobe MC-ICPMS at the TJIGMR, CGS, following the procedure described by Li et al. (2006). Measured $^{87}Sr/^{86}Sr$ and $^{143}Nd/^{144}Nd$ ratios were normalized to $^{86}Sr/^{88}Sr = 0.1194$ and $^{146}Nd/^{144}Nd = 0.7219$, respectively. The reported $^{87}Sr/^{86}Sr$ and $^{143}Nd/^{144}Nd$ ratios were adjusted to the NBS SRM 987 standard $^{87}Sr/^{86}Sr = 0.71025$ and the Shin Etsu JNdi-1 standard $^{143}Nd/^{144}Nd = 0.512115$, respectively. Sr–Nd isotope results are listed in Table S6.

4. Analytical results

4.1. Geochronology

Most zircons from the MZT gabbroic samples (15D031 and 17KL11) are fine-grained, ranging from 30 μm to 80 μm in length, and are euhedral to subhedral, transparent and colourless. A few grains show slight pinkish colour. Zircons from sample 15D031 were analysed using LA-ICPMS instruments and those from sample 17KL11 were conducted using SHIRIMP method. LA-ICPMS analyses of sample 15D031 yield variable contents of Pb (19–105 ppm), U (242–961 ppm) and variable $^{232}Th/^{238}U$ ratios (0.25–1.93, Table S1). Among the seventeen LA-ICPMS analyses, eight spots yield significantly discordant ages which may be resulted from low contents of ^{207}Pb for these analysed zircons, as they yield similar $^{206}Pb/^{238}U$ ages with other spots. The other nine analyses yield $^{206}Pb/^{238}U$ ages ranging from 493.4 ± 6.2 Ma to 504.8 ± 6.5 Ma (Table S1), and yield mean age of 499.8 ± 5.1 Ma (Fig. 3a). A total of eight spots were carried out by SHRIMP on zircon grains from sample 17KL11 and they exhibit variable contents of Pb (15–85 ppm), U (227–1250 ppm) and variable $^{232}Th/^{238}U$ ratios (0.44–1.08, Table S2) and yield $^{206}Pb/^{238}U$ ages ranging from 488.3 ± 3.6 Ma to 493.9 ± 3.7 Ma. All the concordant analyses by LA-ICPMS and SHRIMP methods yield a mean $^{206}Pb/^{238}U$ age of 491.4 ± 2.5 Ma (Fig. 3b). We conclude that the MZT mafic rocks were emplaced at ca. 500-490 Ma.

A vast majority of zircon grains of the TSHT granites (17KL04 and 18KL06) range from 100 μm to 200 μm in length. They are euhedral, transparent and colourless. In CL images, most zircons show clear oscillatory zoning, indicative of magmatic origin. A total of 32 analyses for the sample 17KL04 yield variable U (353–2435 ppm) and Pb (29–216 ppm) contents and show relatively high $^{232}Th/^{238}U$ ratios (0.32–0.60, Table S2), similar to typical magmatic zircons. Among them, two spots (17KL04-9 and 201704–10) yield slightly younger $^{206}Pb/^{238}U$ ages than others possibly due to loss of radiogenic Pb. The other 30 analyses yield concordant $^{206}Pb/^{238}U$ ages and $^{207}Pb/^{235}U$ ages and form a tight cluster on the concordia diagram with a weighted mean $^{206}Pb/^{238}U$ age of 524.8 ± 2.2 Ma (Fig. 3c, MSWD = 0.93). Twenty-nine analyses for the sample

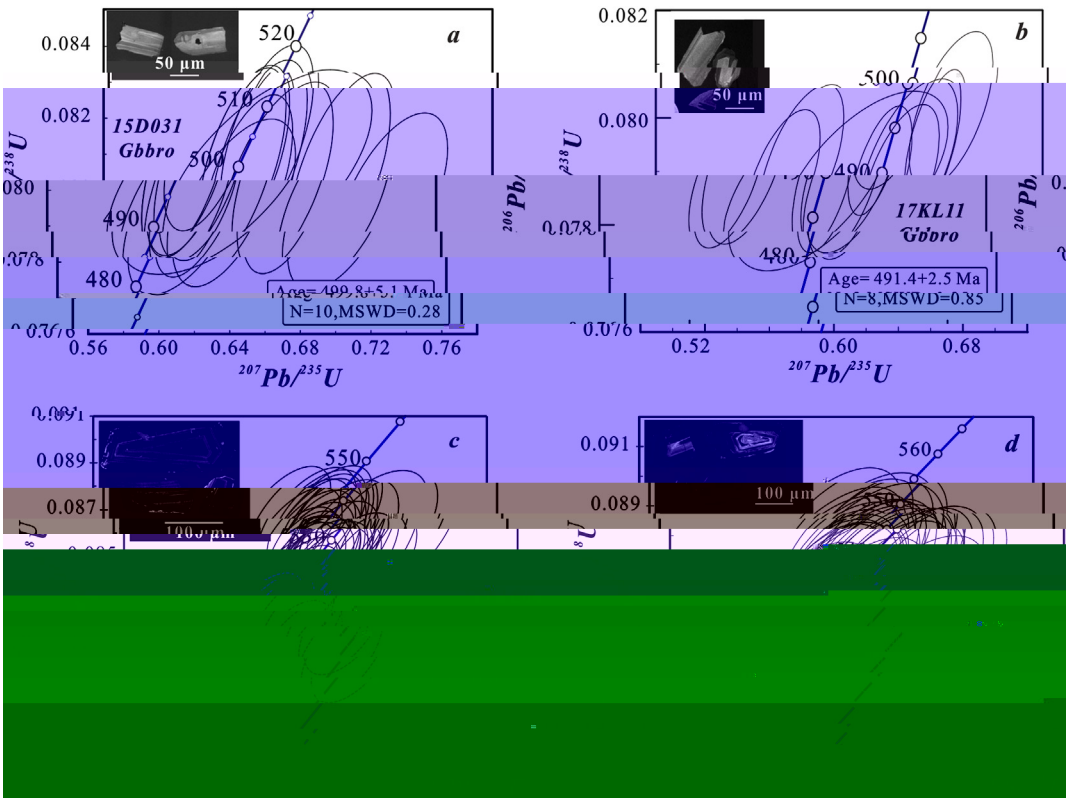

Fig. 3. Concordia plots of zircon U–Pb results of mafic rocks (a, b) from Mazar terrane and granites (c, d) from Tianshuihai terrane. Error ellipses are in 1σ and age uncertainty is quoted at 2σ (mean) level (see detailed discussions in the text).

18KL06 yield variable U (720–3065 ppm) and Pb (66–283 ppm) contents and show relatively high $^{232}Th/^{238}U$ ratios (0.27–1.80, Table S2), similar to typical magmatic zircons. All the 29 analyses yield concordant $^{206}Pb/^{238}U$ ages and $^{207}Pb/^{235}U$ ages and form a tight cluster on the concordia diagram with a weighted mean $^{206}Pb/^{238}U$ age of 532.7 ± 2.5 Ma (Fig. 3d, MSWD = 0.24).

4.2. Mineral geochemistry

A total of 33 analyses were carried on the hornblendes from MZT gabbroic diorites (2016KL17B and 15D071H5). The results show relatively high Si (7.33–7.93) and Ca (1.77–2.03) apfu (atoms per formula unit) and belong to calcic amphibolite according to the classification scheme of Leake et al. (1997). They have low $(Na + K)_A$ (occupancy of Na + K in A-site, less than 0.5), and are mainly actinolite and magnesiohornblende (Fig. 4a). Their $(Na + K)_A$ and $^{[IV]}Al$ (occupancy Al in tetrahedral site) sharply decrease with decreasing TiO_2 (Fig. 4b, c), similar to the secondary trends of amphibole from the Iberian appinites (Molina et al., 2009).

4.3. Whole-rock elemental geochemistry

The MZT doleritic/gabbroic samples have large ranges of SiO_2 (47.88–55.36%), Al_2O_3 (11.48–15.58%), CaO (6.02–14.74%), MgO (2.73–10.78%) and $Fe_2O_3^T$ (9.88–13.39%). Their Na_2O (0.74–5.16%) contents are generally higher than K_2O (0.21–1.30%). Due to variable hydrothermal alteration, we use the immobile incompatible elements to classify the rock types and to decipher their geochemical signatures. On the Nb/Y versus Zr/TiO_2 plot (Fig. 5a), all the samples plot within the sub-alkaline basalt field. On the AFM diagram, they define a typical tholeiitic trend (Fig. 5b). Their $Mg^{\#}$ ranges from 35 to 65 due to crystal fractionation and/or crustal contamination (see following discussions). On the Harker diagrams (Fig. 6), SiO_2, TiO_2, P_2O_5, total REE increase while Cr and Ni decrease with decreasing Mg#, whereas Al_2O_3, $Fe_2O_3^T$, Na_2O, CaO and Zr are not correlated with $Mg^{\#}$. On the chondrite-normalized REE plot, they display enriched LREE patterns with relatively constant $(La/Yb)_N$ (2.67–6.87) ratios (Fig. 7a). Most MZT mafic samples lack significant Eu anomalies ($Eu/Eu^* = 0.81–1.17$). Normalized to primitive mantle, all samples show arc-like patterns with variable enrichments in incompatible trace elements and significant Nb–Ta trough (Nb/La = 0.30–0.44) and variable negative P anomalies (Fig. 7b).

The TSHT mafic intrusions exhibit relatively uniform SiO_2 (46.82–49.68%) and varying Al_2O_3 (14.67–18.16%), CaO (5.47–11.20%), MgO (5.84–10.20%) and $Fe_2O_3^T$ (8.20–11.69%). They are sodium-rich (2.12–4.29%, Na_2O) relative to K_2O (0.23–2.99%). The TSHT mafic rocks have variable Ni (12–156 ppm) and Cr (7–448 ppm) contents (Supplementary Table 3). All samples plot within sub-alkaline basalt field on the Nb/Y versus Zr/TiO_2 plot (Fig. 5a). On the AFM diagram (Fig. 5b), they define a typical tholeiitic signature. On the Harker diagrams (Fig. 6), the Na_2O, TiO_2, P_2O_5, Zr and total REE increase while Cr, Ni and CaO decrease with decreasing $Mg^{\#}$ and SiO_2, Al_2O_3 remain constant. The TSHT mafic intrusions have variable total REE abundances (70.68–225.08 ppm). They display enriched LREE patterns with $(La/Yb)_N$ ratios ranging from 4.71 to 17.4 on the chondrite-normalized REE diagram (Fig. 7c). Most TSHT mafic samples show slightly negative to positive Eu anomalies ($Eu/Eu^* = 0.95–1.29$). All samples exhibit arc-like signatures with variable enrichment in incompatible trace elements and are characterized by negative Nb–Ta anomalies (Nb/La = 0.29–0.49) on the primitive mantle- normalized spider diagram (Fig. 7d).

The TSHT granites are featured by high contents of SiO_2 (75.14–79.57%). They have variable K_2O (0.38–6.55%) and Na_2O (3.11–6.62%), with the total alkaline ranging from 6.04% to 9.66%.

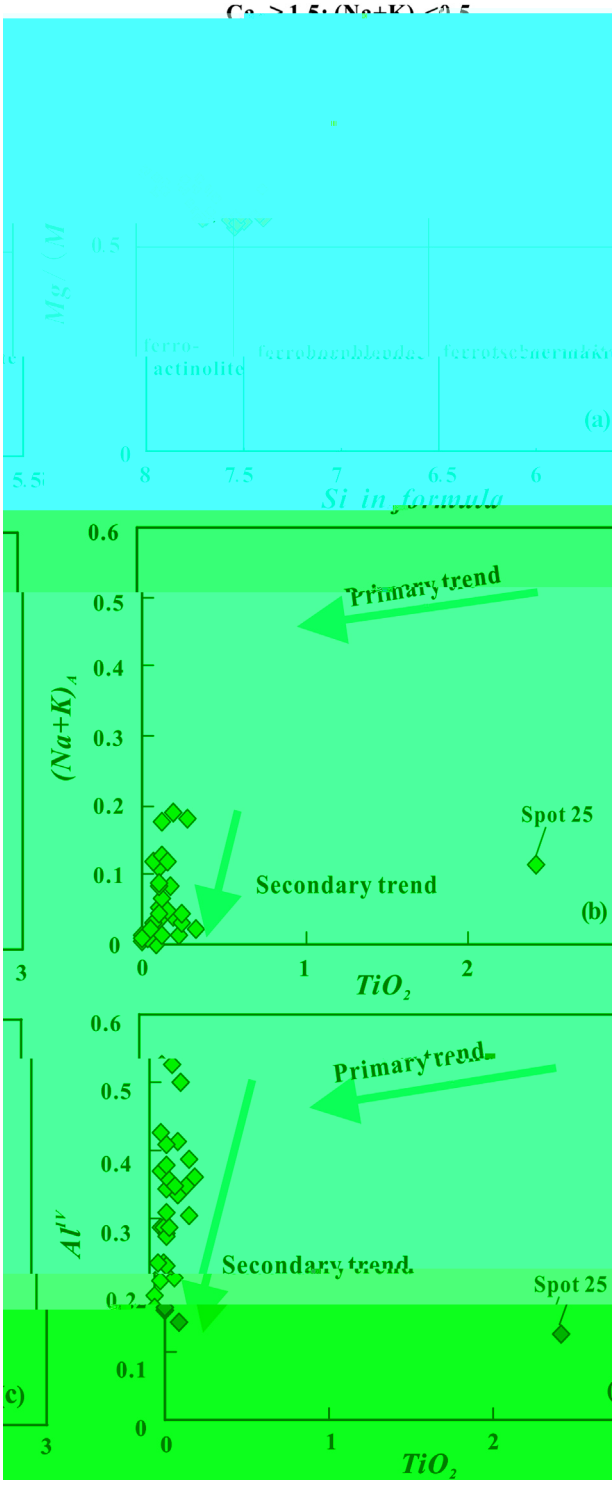

Fig. 4. (a) Classification of hornblende (Leake et al., 1997); (b) TiO_2 (%) vs. Al^{IV} and (c) TiO_2 (%) vs. $(Na + K)_A$ diagrams of the hornblende showing the secondary trends.

Fig. 5. (a) Nb/Y vs. Zr/TiO_2 classification, (b) AFM and (c) TAS diagrams of the dolerite-gabbro and granite from Mazar Terrane-Tianshuihai Terrane.

On the TAS diagram (Fig. 5c), they plot into the field of granite. They have low contents of Al_2O_3 (11.80–13.85%), TiO_2 (0.05–0.15%), MnO_2 (0.01–0.03%), MgO (0.06–0.52%) and P_2O_5 (0.01–0.02%). Major elements define their peraluminous signature with A/NK ranging from 1.10 to 1.24 and A/CNK ranging from 1.04 to 1.13. The TSHT granites have total REE abundances ranging from 120 to 241 ppm. They exhibit a relatively flat REE pattern on the chondrite-normalized REE diagram (Fig. 7e), with $(La/Yb)_N$ ratios ranging from 2.61 to 7.19 and highly negative Eu anomalies ($Eu/Eu^* = 0.02–0.09$), likely due to plagioclases fractionation. Normalized to primitive mantle, all samples show enrichments in large ion lithophile elements such as Rb, Th, La and depletions in Ba, Sr, P, Ti and Eu (Fig. 7f).

4.4. Zircon in situ Lu–Hf isotopic compositions

A total of 57 in situ Lu–Hf isotopic analyses were carried on the dated zircons from two TSHT granitic samples (17KL04 and 18KL06,

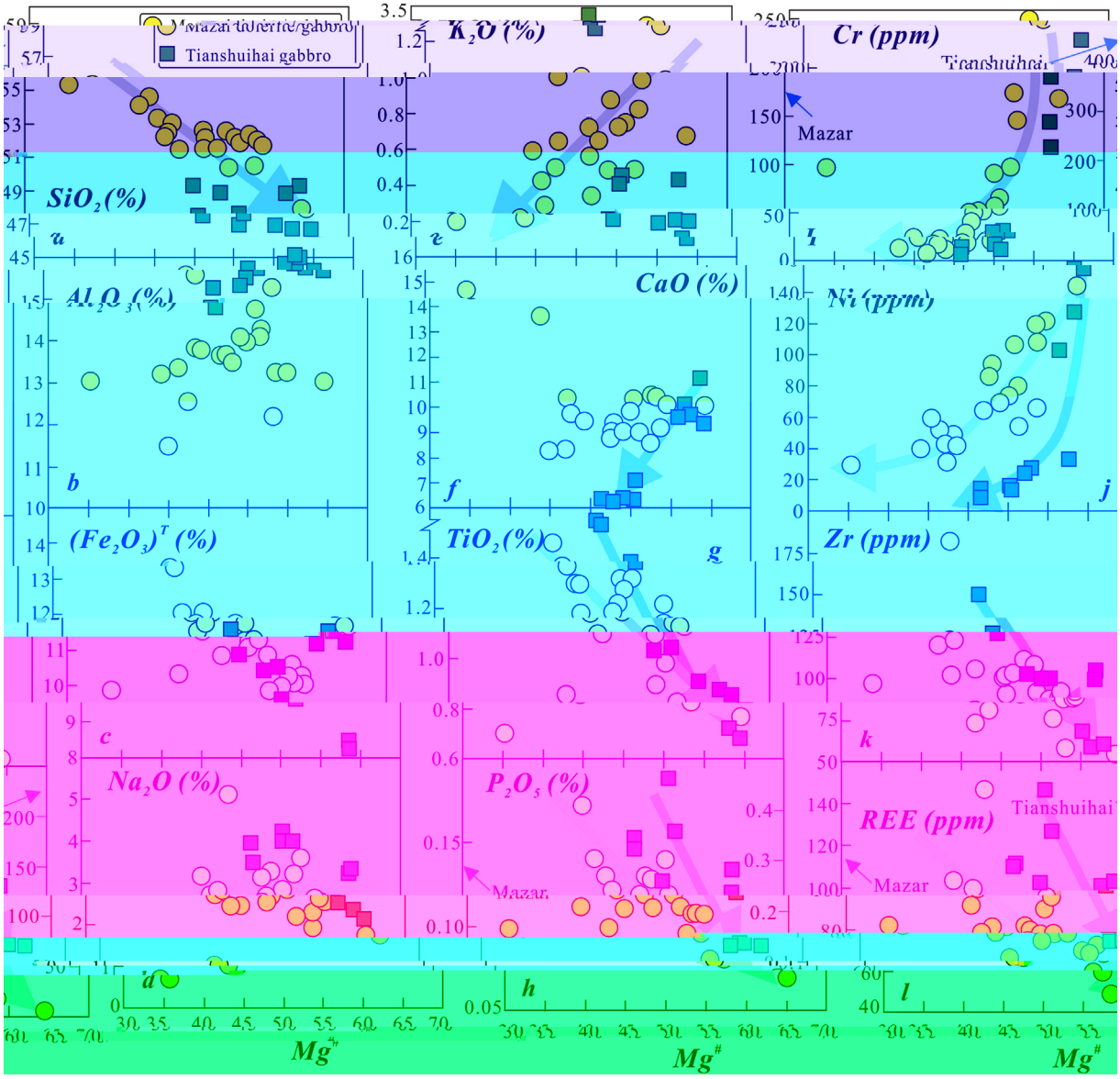

Fig. 6. Harker diagrams for the Cambrian mafic intrusive rocks from Mazar- Tianshuihai terrane.

Table S5). All analyses show positive initial $\varepsilon_{Hf}(t)$ values ranging from 2.6 to 9.2 (mostly between 4 and 8) and exhibit a general Gaussian distribution (peaks at ~5, Fig. 8a) and Meso-Proterozoic two stage model age (T_{DM2}) ranging from 905 to 1324 Ma (Fig. 8b).

4.5. Sr—Nd isotopic compositions

The MZT dolerite/gabbro samples have negative $\varepsilon_{Nd}(t)$ values (−12.90 – -9.71) and variable initial $^{87}Sr/^{86}Sr$ values (0.7107–0.71517, Table S6, Fig. 9a). The TSHT mafic rocks have positive $\varepsilon_{Nd}(t)$ values ranging from 2.74 to 3.60, and their initial $^{87}Sr/^{86}Sr$ values ranging from 0.70597 to 0.70847. As for the Cambrian TSHT granites, they exhibit $\varepsilon_{Nd}(t)$ values ranging from −0.39 to 1.08, and initial $^{87}Sr/^{86}Sr$ values ranging from 0.7039 to 0.71229. We notice the significant decoupling between the whole-rock Nd and Sr isotope compositions for the MZT mafic rocks, which could be ascribed to post-emplacement hydrothermal alteration (e.g., McCulloch et al., 1981) as demonstrated by the thin section observations and the hornblende chemical compositions. Thus, the Sr isotopes of the MZT mafic rocks are unsuitable for further discussions on the petrogenesis of these rocks. On the $\varepsilon_{Nd}(t)$ vs. $\varepsilon_{Hf}(t)$ diagram (Fig. 9b), the TSHT granites show broadly coupled whole-rock Nd and zircon Hf isotopes.

5. Discussions

5.1. Petrogenesis of the mafic rocks

5.1.1. Hydrothermal alteration

As indicated by their high LOI (mostly higher than 2%), secondary minerals observed in thin sections and apparently secondary trends for the amphibole (Fig. 4b, c), the MZT-TSHT mafic rocks underwent variable degrees of alteration after emplacement, which may have changed the concentration of some incompatible elements due to their enhanced mobility. Since Zr is considered to be immobile during low-grade hydrothermal alteration and metamorphism of igneous rocks, it has been used as a reference for studying the mobility of other trace elements (Pearce et al., 1992). We investigated the correlations between Zr and other elements (figures not presented). The results indicate that TiO_2, Nb, Th, Hf, Y,

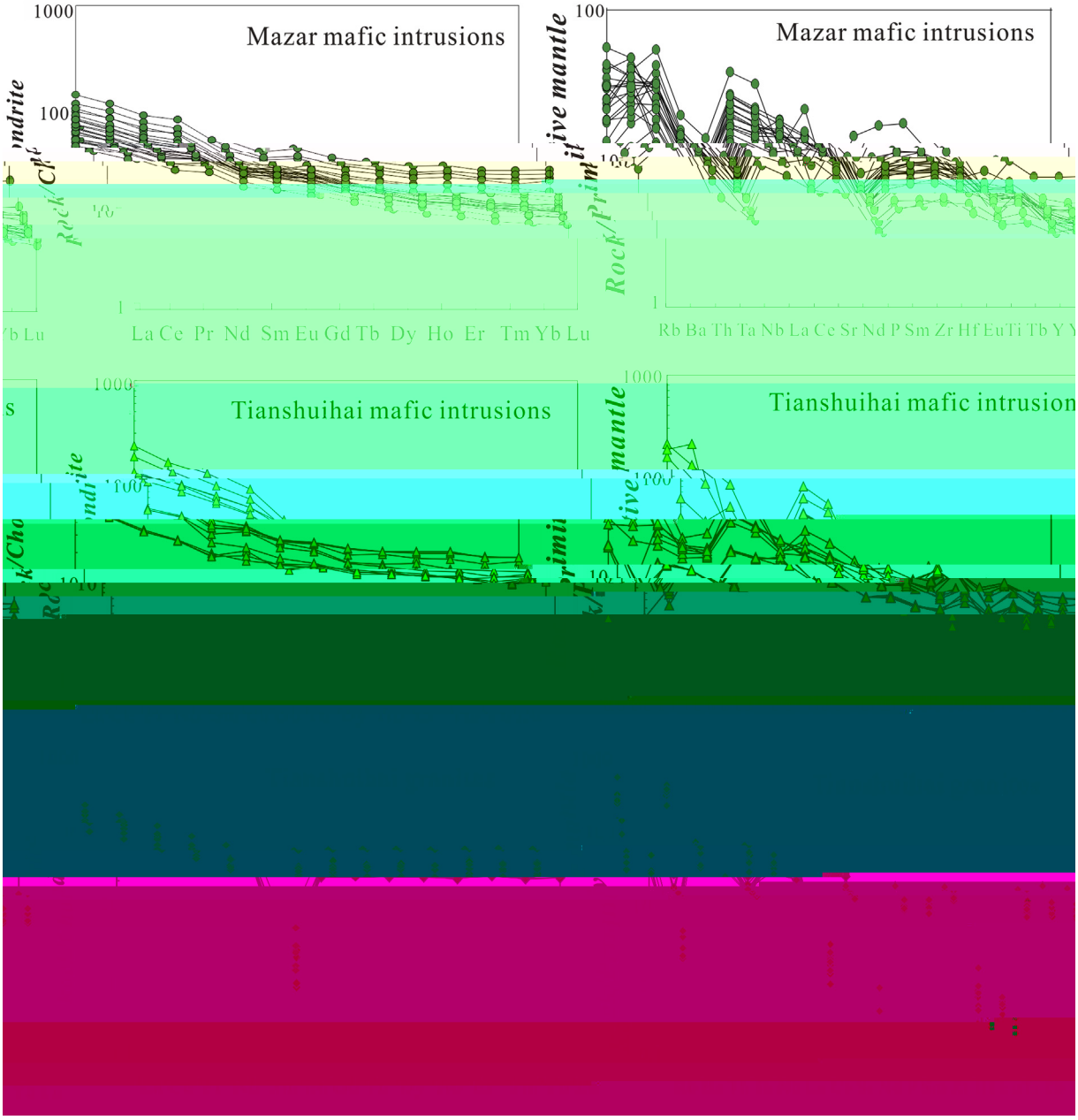

Fig. 7. Chondrite-normalized REE patterns and primitive mantle- normalized incompatible trace elements spider diagrams for mafic and granitic intrusions from Mazar- Tianshuihai terrane. All the normalizing values are from Sun and McDonough (1989).

Ta and REE correlate well with Zr, suggesting relative immobility of these elements during post-emplacement processes. Some LILEs, such as Ba, Rb and Sr, however, show no correlation with Zr, indicating their mobility. Thus, we conclude that alteration processes have not significantly affected high field strength elements (HFSE: Th, Nb, Zr, Hf, Ti, Y) and REEs. Their variations could be ascribed to magmatic processes and can be used for petrogenesis discussions.

5.1.2. AFC process

The analysed mafic rocks have variable MgO (2.73–10.78% for MZT and 5.84–10.50% for TSHT), $Mg^{\#}$ (35–65 for MZT and 51–65 for TSHT), Cr (5.88–255 ppm for MZT and 20.0–448 ppm for TSHT), Ni (31.9–145 ppm for MZT and 12.1–156 ppm for TSHT) and total REE abundances (41.5–148 ppm for MZT and 70.7–225 ppm for TSHT), indicating that they crystallized from evolved rather than primitive magmas, probably due to assimilation and fractional crystallization (AFC) processes. As shown in the Harker diagrams (Fig. 6), these analysed samples exhibit distinct positive correlations between Cr and $Mg^{\#}$ (Fig. 6i), Ni and $Mg^{\#}$ (Fig. 6j), indicating fractionation/cumulation of olivine or/and clinopyroxene. The distinct clinopyroxene-plagioclase control trend in the Pearce elemental ratios diagram (Fig. 10a) confirmed the fractionation/cumulation of clinopyroxene and plagioclase. The negative correlations between Fe_2O_3 and TiO_2 concentrations and $Mg^{\#}$ are indicative of fractional crystallization/cumulation of Fe–Ti oxides. AFC process can produce a positive correlation between $\varepsilon_{Nd}(t)$ and $Mg^{\#}$. The slightly positive correlation between the $\varepsilon_{Nd}(t)$ and $Mg^{\#}$ for the MZT mafic rocks argues for crustal contamination before final crystallization of the MZT mafic magma (Fig. 10b). As for the mafic rocks from TSHT, no significant correlation is observed

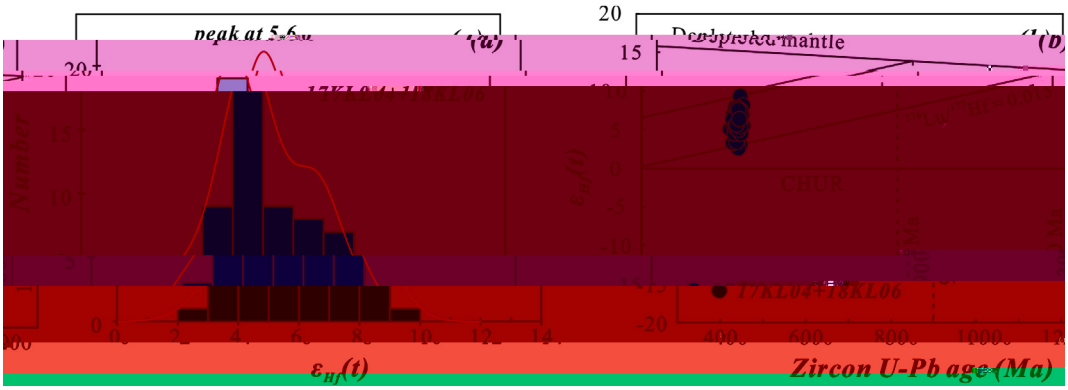

Fig. 8. Zircon $\varepsilon_{Hf}(t)$ spectra (a) and zircon U–Pb age vs. $\varepsilon_{Hf}(t)$ diagrams (b) of the Cambrian granitic intrusions from Tianshuihai Terrane.

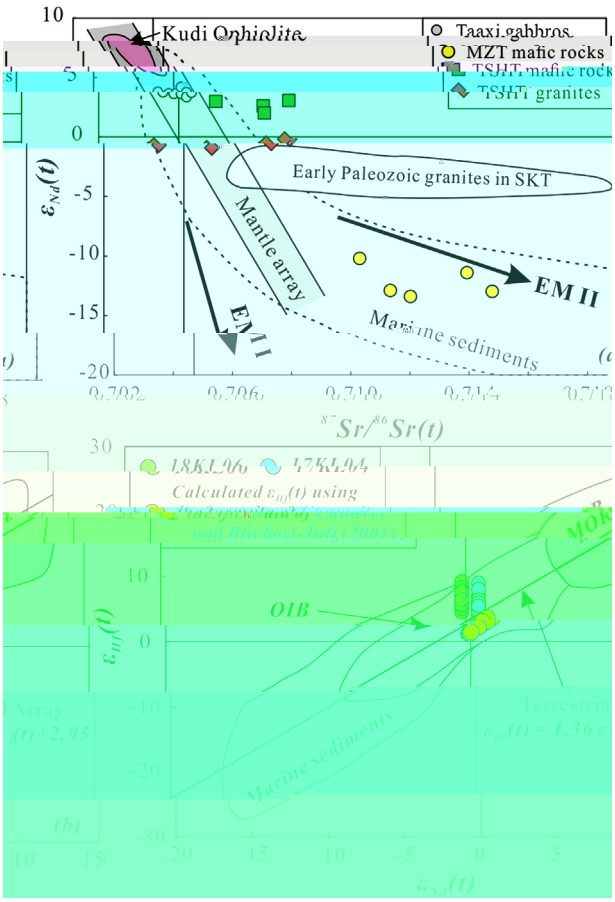

Fig. 9. (a) Whole-rock Sr–Nd isotopic diagram of the Cambrian mafic and granitic intrusions from Mazar-Tianshuihai Terrane. The Taaxi gabbros are from Zhang et al. (2018d); The South Kunlun Terrane (SKT) granites are from Zhu et al., 2017; Liao et al., 2010, Wang et al. (2017), Liu et al. (2014); The marine sediments are from Hofmann, 2003; Kudi Ophiolite are from Pan, 1996. (b) Whole-rock $\varepsilon_{Nd}(t)$ vs. zircon $\varepsilon_{Hf}(t)$ diagram of the Cambrian granitic intrusions from Tianshuihai Terrane, showing coupled Nd–Hf isotopic compositions. The terrestrial array and the fields for middle ocean ridge basalt (MORB), oceanic island basalt (OIB) and global sediments are from Vervoot et al., 1999..

between the $\varepsilon_{Nd}(t)$ and $Mg^{\#}$, indicating insignificant crustal contamination (Fig. 10b). Crustal contamination could simultaneously decrease $Mg^{\#}$ and Nb/La ratios which could produce a positive correlation between the $Mg^{\#}$ and Nb/La. This conclusion is supported by the slight positive correlation and no significant correlation between the $Mg^{\#}$ and Nb/La for the MZT and TSHT mafic rocks, respectively (Fig. 10c). The $(La/Ta)_N$ vs. $(Th/Ta)_N$ diagram (Fig. 10d) indicates that the contaminated components for the MZT mafic rocks was the upper crust.

Therefore, we conclude that the analysed mafic samples from TSHT have not undergone significant crustal contamination, whereas those Cambrian rocks from MZT have been contaminated by the upper crust component in this region.

5.1.3. Magma sources

The MZT and TSHT are two distinct Precambrian basements in the WKOB, i.e., the Archean MZT (Zhang et al., 2018b) and the Neoproterozoic TSHT (Zhang et al., 2018c). The different signatures of the Precambrian basements for the MZT and TSHT lead us to conclude that these two terranes possess different Cambrian mantle sources. The mafic rocks from the TSHT have depleted whole-rock Nd isotopic compositions ($\varepsilon_{Nd}(t) = 2.74$ to 3.60), and exhibit arc-like whole-rock elemental compositions, such as significant Nb–Ta trough, enrichment of LREEs, LILEs and depletion of HREEs and HFSEs (Fig. 7, Rudnick and Gao, 2003). The decoupling of the depleted Nd isotopes and the enriched LREEs and LILEs share most features of the E-MORB and some OIBs (e.g., Zhang et al., 2018d). Such features can be ascribed to crustal contamination (Rudnick and Gao, 2003), hybridization of magma sources by recycled terrigenous sediments or fluid metasomatism in the subduction zone (e.g., Hawkesworth et al., 1993) or crystallization of Ti-bearing minerals (such as rutile and Ti-bearing amphibole) (e.g., Huang et al., 2010). As mentioned above, crustal contamination can be ruled out. Although fractionation/accumulation of Ti-bearing minerals might have occurred as mentioned above, this was not the key reason to generate the Nb–Ta trough of the mafic rocks from TSHT, because of the positive correlation between the TiO_2 and Nb/La ratios (figure not shown). Thus, the mantle source for the parent magma of the TSHT mafic rocks was most likely metasomatized or enriched by melts or fluids in a subduction zone (e.g., Hawkesworth et al., 1997). Nb/U and Ta/U ratios are commonly used to identify the injection of crustal material into mantle source or crustal contamination (e.g., Hofmann, 1988). The Nb/U and Ta/U ratios of the TSHT mafic rocks are 7.1–23.3 and 0.4–1.3, significantly lower than those of the OIB and MORB (Nb/U~47 and Ta/U~2.7, Hofmann, 1988). The low ratios of Nb/U and Ta/U feature of the TSHT mafic rocks argue for significant injection of crustal materials into the depleted mantle sources for the TSHT mafic rocks, which might be due to subduction processes. In light of their depleted whole-rock Nd isotopic compositions, we propose that they were originated in the initial subducting setting of the southward subduction of the Proto-Tethys Ocean.

Although having undergone upper crust contamination, the MZT mafic rocks with variable $Mg^{\#}$ numbers exhibit similar Nb/La

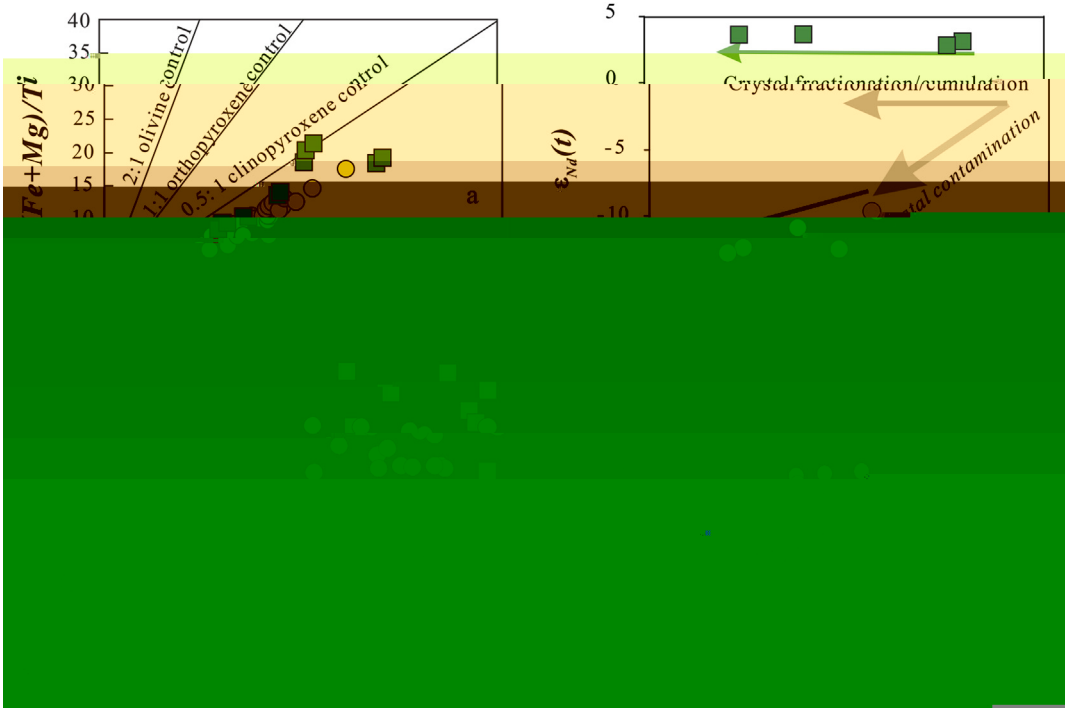

Fig. 10. (a) Si/Ti vs. (Mg + Fe)/Ti (molar ratios) diagram of MZT-TSHT mafic rocks showing accumulation of clinopyroxene and plagioclase; (b) $Mg^{\#}$ vs. $\varepsilon_{Nd}(t)$, (c) $Mg^{\#}$ vs. Nb/La and (d) $(La/Ta)_N$ vs. $(Th/Ta)_N$ diagrams illustrating upper continental crust contamination trends for the MZT mafic rocks, and no significant contamination for the TSHT mafic rocks. UCC – upper continental crust; LCC – lower continental crust.

ratios (0.30–0.46). Thus, their incompatible ratios could broadly reflect their primitive geochemical signatures. The REE and incompatible element distribution patterns of MZT mafic intrusions broadly exhibit arc basalt signatures such as their significant Nb–Ta trough (Fig. 7), enrichment of LREEs, LILEs and depletion of HREEs and HFSEs (Rudnick and Gao, 2003, Fig. 7). Furthermore, their HFSE ratios, such as Th/La and Nb/Th, are also comparable with those of primitive arc basalts (Fig. 11, OIBs, primitive arc basalt and average continental crust are from Sun and McDonough, 1989 and Rudnick and Gao, 2003, respectively). Among the MZT mafic rocks, the sample with least negative initial Nd isotopic composition (−9.71) has high $Mg^{\#}$ (59), which argues for an isotopically enriched mantle source for the primary magma of the MZT mafic rocks. We deduce that they were derived from an enriched sub-continental lithospheric mantle (SCLM). As a matter of fact, the Archean MZT possesses a long-term enriched SCLM according to the whole-rock $\varepsilon_{Nd}(t)$ values of the Archean mafic volcanic rocks (−11.9 to −9.3, recalculated to 490 Ma, Ji et al., 2011), which is consistent well with the MZT mafic rocks. Partial melting of an initially cold SCLM could not occur unless plenty of subduction-related fluids modified the mantle source (Ringwood, 1974). This may be related to the continuously (530–490 Ma) southward subduction of the Proto-Tethys Ocean.

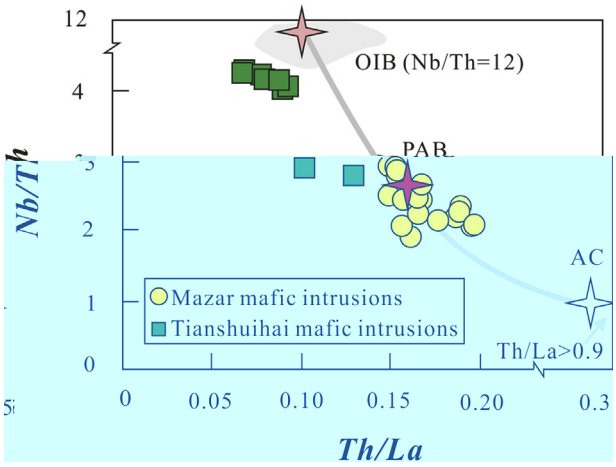

Fig. 11. Th/La vs. Nb/Th diagram. The MZT mafic rocks cluster around primitive arc basalts (PAB) and the TSHT mafic rocks plot between oceanic island basalt (OIB) and PAB. OIB, PAB and average continental crust (AC) are after Sun and McDonough (1989), Rudnick and Gao (2003), respectively.

The TSHT mafic rocks exhibit positive whole-rock Nd isotopic compositions whereas the MZT mafic rocks display much more enriched whole-rock Nd isotopic compositions ($\varepsilon_{Nd}(t) = -12.90$ – -9.71). From the TSHT mafic rocks (ca. 530 Ma) to the MZT mafic rocks (ca. 490 Ma), the mantle sources of the mafic rocks transformed from a depleted mantle to an enriched SCLM, which might be resulted from increasing metasomatized degree of the slab subduction. This conclusion is further supported by the relatively higher Th/Yb ratios at a given Nb/Yb for the MZ-TSHT mafic rocks. All MZT mafic rocks plot into the field of continental arc and those TSHT mafic rocks plot between the field of continental arc and the mantle-array on the Nb/Yb vs. Th/Yb diagram (Fig. 12). Comparing with the binary diagram, the triangular diagram would be influenced less by crystal fractionation. On the Nb–Zr/4-Y diagram (Fig. 13), the TSHT mafic rocks are mostly plot in the field of within plate tholeiitic basalts, with some shift to within plate alkaline basalts, while the MZT mafic rocks plot into the fields of volcanic arc basalts.

To sum up, the Cambrian TSHT mafic rocks were derived from a depleted mantle source in an initial subduction setting, whereas the Cambrian MZT mafic rocks were most likely derived from a subduction metasomatized SCLM wedge in an arc setting.

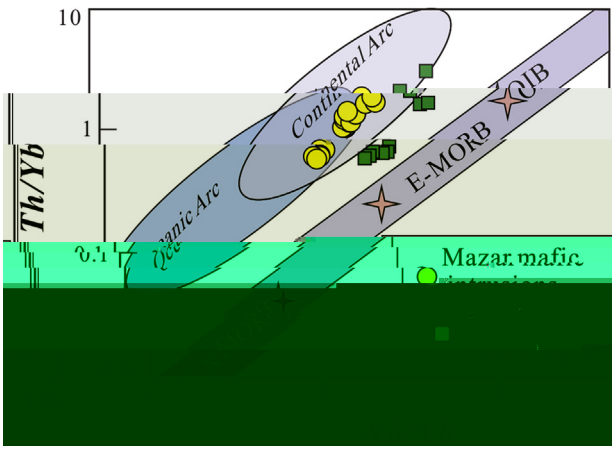

Fig. 12. Nb/Yb vs. Th/Yb diagram showing continental arc feature for the MZT mafic rocks and shift between E-MORB and OIB to continental arc (see details in the text).

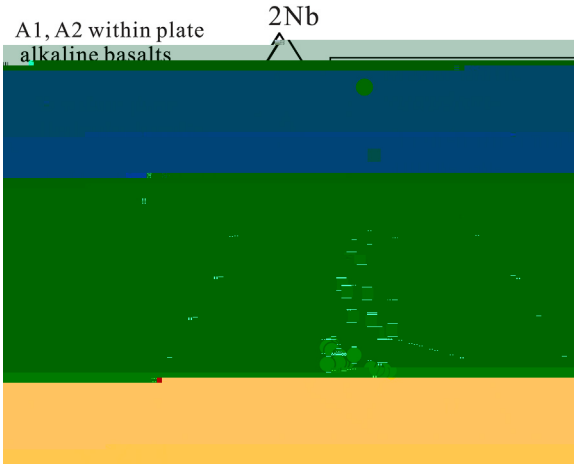

Fig. 13. Nb–Zr/4-Y ternary diagram illustrating the volcanic arc basalts signature for MZT mafic intrusions and within plate tholeiitic basalts signature for the TSHT mafic intrusions (see details in the text).

5.2. Petrogenesis of the TSHT granites

The TSHT granites have extremely high contents of SiO_2 (75.14–79.57%) and highly negative Eu anomalies ($Eu/Eu^* = 0.02–0.09$) and are depleted in Ba, Sr, P in the primitive mantle normalized diagrams (Fig. 7f). They exhibit low ratios of $1000*Ga/Al$ (2.23–2.65) and $(Na_2O + K_2O)/CaO$ (5.15–9.45), and low contents of Zr (96.6–146 ppm) and Zr + Nb + Ce + Y (207–345 ppm), both lower than the lower limit of the typical A-type granites (Collins et al., 1982; Whalen et al., 1987). Most TSHT granites plot into the fractionated granite field on the diagram of Zr + Nb + Ce + Y vs. $(Na_2O + K_2O)/CaO$ (Fig. 14a). These characteristics of the TSHT granites reveal that they are highly fractionated granites, as evidenced by their low contents of $Fe_2O_3^T$ and MgO. Unfractionated granites usually have relatively constant ratios of twin HFSE elements, such as Zr/Hf and Nb/Ta (Green, 1995). While those ratios will decrease obviously when the magma system experiencing intensive fractionation (e.g., Pérez-Soba and Villaseca, 2010). The TSHT granites show low ratios of Zr/Hf (22.5–28.9) and Nb/Ta (4.25–7.90) relative to typical granites (38 for Zr/Hf and 17 for Nb/Ta), which is consistent with strong differentiation.

The TSHT granites show relatively low contents of Al_2O_3 (11.80–13.85%) and are weakly peraluminous (mostly lower than 1.10), which is distinct from typical S-type granites (Chappell, 1999). As a common accessory mineral in magmatic rocks, apatites have different solubility in different magma system (e.g., Li et al., 2007). Apatites have very low solubility in metaluminous to weakly peraluminous magma system and crystallize early during the fractionation of magma system, which result in a negative relationship between P and SiO_2. While in the strong peraluminous magma, the apatites show an opposite behavior and lead to a positive or remain unchanged as the SiO_2 increase (Wolf and London, 1994). This different behavior of apatites in metaluminous to weakly peraluminous magma and peraluminous magma can be used to discriminate I- and S-type granites (Wu et al., 2003). The TSHT granites exhibit very low contents of P_2O_5 ($\leq$0.02%, Fig. 14b), indicative of I-type granite affinity. In addition, all TSHT granitic samples plot into I-type granite field on the Zr vs. TiO_2 diagram (Fig. 14c). Therefore, we conclude that the Cambrian TSHT granites are highly-fractionated I-type granites.

The extremely negative Eu anomalies ($Eu/Eu^* = 0.02–0.09$) and low contents of Sr (21.9–71.5 ppm) suggest fractional crystallization of plagioclase. The apparently negative Ba, Sr, P and Ti anomalies in the primitive-mantle-normalized trace elements and REE variation diagrams for the TSHT granites (Fig. 7) indicate fractionation of plagioclase, apatite and Fe–Ti oxides during magma evolution. Furthermore, plot of process identification diagram on log Ba vs. log Rb (Fig. 14d) yield trends of crystal fractionation of plagioclase and K-feldspar, which is consistent with the negative correlation between log Eu and log Ba (Fig. 14e). The TSHT granites show low total contents of REEs (low to 120 ppm), which could be ascribed to fractional crystallization of REE-enriched accessory minerals, such as apatite and monazite. The La vs. $(La/Yb)_N$ diagram (Fig. 14f) reveals that the REEs variations in the TSHT granites were likely controlled by crystallization of monazite and/or allanite.

The TSHT granites occur closely temporally and spatially related to the TSHT mafic rocks, suggesting the former could be formed by intensive fractional crystallization of the later. However, their distinct whole-rock Nd isotopic compositions ($\varepsilon_{Nd}(t)$ values of the granites ranging from −0.39 to 1.08, while for the doleritic gabbro from 2.74 to 3.60), does not favour this conclusion. Considering their ultra-high SiO_2 contents (75.14–79.57%), we prefer that they were originated by partial melting of crustal sources. The positive zircon $\varepsilon_{Hf}(t)$ values (2.6–9.2, peak at 5.6) and positive to negative whole-rock Nd isotopic compositions suggest that they were originated from a juvenile crust source region. They exhibit broadly coupled Nd–Hf isotopic compositions (Fig. 9b), with two-stage zircon Hf model ages ranging from 0.91 to 1.32 Ga (Table S5) and two-stage model ages of whole-rock Nd isotopes ranging from 1.07 to 1.21 Ga (Table S6). The consistent zircon Hf and whole-rock Nd two-stage model ages of the TSHT granites suggest a Mesoproterozoic source region. The concurrent hot mantle-derived magma represented by the TSHT mafic rocks may provide heat source for partial melting of the Mesoproterozoic lower crust.

5.3. Tectonic implications

The word “Tethys”, first defined by Suess (Suess, 1893), was initially introduced into geology to describing a paleo-ocean spread in Tibet, Himalaya and Alps. Nowadays, the meaning of Tethys has changed in both spatial and temporal distribution comparing the initial meaning of Suess’ Tethys. The Tethys can be subdivided into the Proto-Tethys, the Paleo-Tethys, Meso-Tethys and Ceno-Tethys according to its evolutionary periods (Metcalfe, 2013). The Proto-Tethys, existed during the Late Neoproterozoic to Early Paleozoic, represented the paleo-ocean separated the Tarim-Alex-North China Block and the Eastern Gondwana (see Zhao et al., 2018). While the Paleo-Tethys, maybe result by southward subduction of the Paleo-Asia Ocean, mainly existed during the Late Paleozoic to Triassic (Han et al., 2016; Metcalfe, 2013).

The final closure of the Mozambique Ocean between East Gondwana and West Gondwana at ca. 540–530 Ma formed the Great Gondwana (Fig. 15a, Collins and Pisarevsky, 2005; Li et al., 2008), as evidenced by the palaeomagnetic studies (Meert and Van der Voo, 1996), causing the final docking of India to Australia-East Antarctica along the Pinjarra Orogen (Boger and Miller, 2004; Collins and Pisarevsky, 2005). Episodic bioprovince connections with East Gondwana during the Early-to mid-Paleozoic indicated that the micro-continents distributed in Eastern Asia, including the Tarim, Qaidam, Qilian, South China Block (SCB), North China Block (NCB), Alex, Sibumasu and Indochina, were located nearby Australia (Fig. 15b, Metcalfe, 2011, 2013).

The Archean MZT and late-Neoproterozoic TSHT are two newly identified Precambrian basements in the WKOB (Zhang et al., 2018c, d). Although the MZT and the TSHT are different in age, they are all confirmed Precambrian basements in the WKOB. Considering the similarity of the Early Paleozoic accretionary complex of BKG and Saitula Group (Zhang et al., 2018a, c), distributed to the north of the MZT and TSHT, respectively, it is quite possible that the MZT and TSHT are as a whole before the early Cambrian (ca. 530 Ma). This conclusion is further supported by the paleogeographic evidence to the southern margin of the Tarim Block (Huang et al., 2011). According to the paleogeographic reconstruction of Li et al. (2018), we place the MZT-TSHT between the Tarim and Eastern Gondwana (Fig. 15b). The MZT possesses the Archean (ca. 2.5 Ga) bimodal meta-igneous rock overprinted by ca. 2.0 Ga metamorphism and Neoproterozoic (ca. 840 Ma) granitic magmatism (Zhang et al., 2018b), which share most similarity to the Archean Kongling complex in the SCB (Zhang and Zheng, 2013). Further, the detrital zircons of the flysch-like sedimentary sequences in the TSHT shared similar age spectra to the late Neoproterozoic sequence from SCB (Hu et al., 2016; Zhang et al., 2015, 2018c). Precambrian rock assembages, phases of igneous activities and metamorphism of the MZT-TSHT share most features to those of the SCB, which argued that this terrane was continental fragments detached from SCB during the breakup of the Rodinia Supercontinent. The BKG was an early Cambrian (530–508 Ma, Zhang et al., 2018a

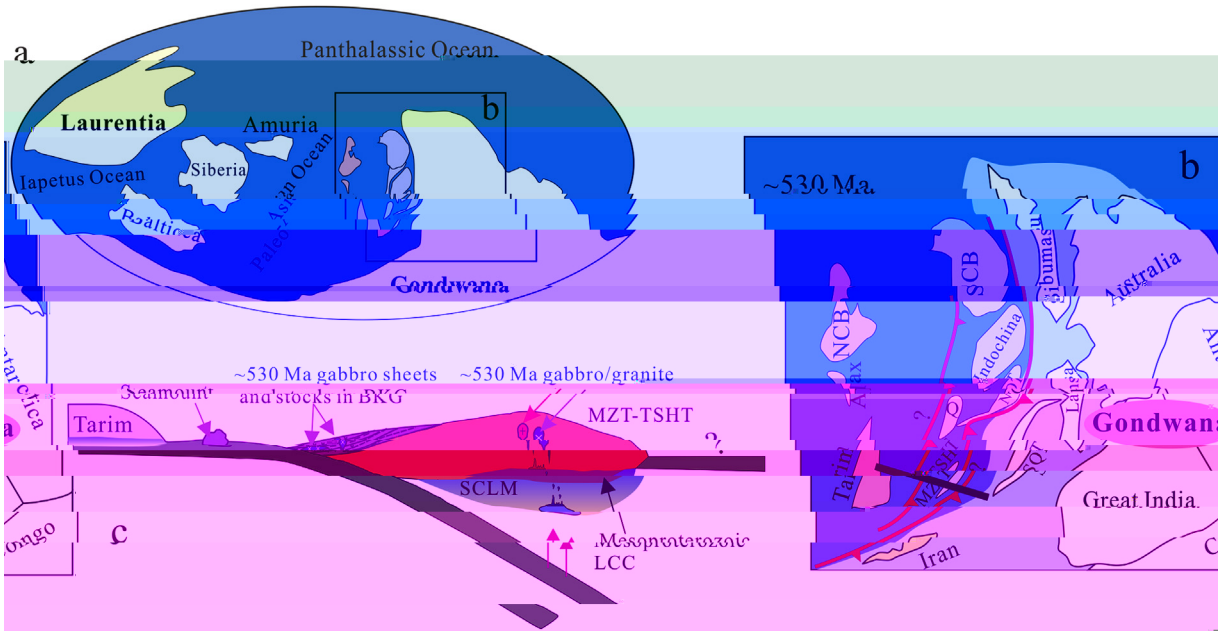

Fig. 15. Early Cambrian (~530 Ma) global continental/micro-continental blocks distribution (a) and possible distribution of the blocks at the northern fringe of Gondwana (b, Modified from Li et al., 2018; Metcalf et al., 2011, 2013). (c) Cartoon model showing the formation of Cambrian dolerite-gabbros in the MZT-TSHT and the initiation of Proto-Tethys oceans subduction at ca. 530 Ma (the thickness of the SCLM and crust is not exactly scaled). BKG—Cambrian Bulunkuole Group; Q—Qaidam; SCB—South China Block; NCB—North China Block; SQT—South Qiangtang; NQT—North Qiangtang; MZT-TSHT—Mazar Terrane-Tianshuihai Terrane. See details in the text.

gabbro intrusions in the TSHT south to the BKG was coeval with those gabbro sheets and stocks emplaced in the lower part of the BKG (Zhang et al., 2018d), which formed the initial magmatic arc of the southward subduction of the Proto-Tethys Ocean (Fig. 15c). The continuous southward subduction of the Proto-Tethys Ocean led to the metasomatism of the SCLM beneath the MZT. Partial melting of the metasomatized enriched mantle source (SCLM) generated the mafic intrusions in the MZT.

Voluminous early Paleozoic granites emplaced in the SKT and the TSKT during 510—400 Ma (Jiang et al., 2002, 2008; Zhang et al., 2018a, 2018b). These granites show variable geochemical compositions, including the 430 Ma adakitic rocks (Ye et al., 2008; Wang et al., 2017), which may be resulted from partial melting of the thickened lower crust (Wang et al., 2017). The thickening of the continental crust in an orogenic belt can be ascribed to the continent-continent collision, such as the Dabie Orogenic Belt and Tibetan Plateau (Chung et al., 2003; Wang et al., 2007), indicating that the final collision between the Tarim Block and East Gondwana was earlier than 430 Ma. Our results, coupled with the occurrence of ca. 440 Ma amphibolite-facies metamorphism of the SKT, document that the accretion between Tarim and TSHT was finished at ca.440 Ma (Zhang et al., 2018c). The closure of the Proto-Tethys Ocean led to the final assemblage of the blocks in the Northern Tibet and Asia, including the Tarim, MZT-TSHT, Qaidam, SCB, Indochina, etc., to the northern margin of the East Gondwana (Metcalfe, 2011, 2013).

6. Conclusions

(1) The granitic intrusions in Tianshuihai Terrane were emplaced at ca. 530 Ma, coeval with the dolerite-gabbros in this area and the gabbro sheets and stocks emplaced into the lower part of the Cambrian accretionary wedge. The dolerite-gabbro from the Mazar Terrane was emplaced at ca. 500—490 Ma.

(2) The doleritic/gabbroic intrusions in Tianshuihai Terrane were derived from a depleted mantle source in an initial subduction setting; whereas the mafic intrusions in Mazar Terrane were generated from a sub-continental lithospheric mantle source in an arc setting.

(3) A Cambrian magmatic arc, genetically related to the southward subduction of the Proto-Tethys Oceans during 530—490 Ma, was developed along the Mazar-Tianshuihai terrane. The final closure of the Proto-Tethys Oceans occurred at ca. 440 Ma, which led to the terranes along the northern margin of the Tibet Plateau and East Asia docked to the East Gondwana.

Acknowledgements

We sincerely thank Mr. Wen-Hua Ji for his help with field work and supplying the 1/50000 geological maps. We are grateful to Dr. Wei Xie for his assistance with SHRIMP zircon dating and to Dr. Jian Zhang for LA-MC-ICPMS zircon dating and in situ Lu—Hf isotope analyses. This project is funded by the National 305 Project of China (2018A03004-1, 2015BAB05B01-1) and the Fundamental Research Funds for the Central Universities (2019B18914).

Appendix A. Supplementary data

Supplementary data to this article can be found online at https://doi.org/10.1016/j.lithos.2019.105226.

References

Boger, S.D., Miller, J.M., 2004. Terminal suturing of Gondwana and the onset of the Ross—Delamerian orogeny: the cause and effect of an Early Cambrian reconfiguration of plate motions. Earth Planet. Sci. Lett. 219, 35—48.

Chappell, B.W., 1999. Aluminium saturation in I- and S-type granites and the characterization of fractionated haplogranites. Lithos 46, 535—551.

Chung, S.L., Liu, D.Y., Ji, J.Q., Chu, M.F., Lee, H.Y., Wen, D.J., Lo, C.H., Lee, T.Y., Qian, Q., Zhang, Q., 2003. Adakites from continental collision zones: melting of thickened lower crust beneath southern Tibet. Geology 31, 1021—1024.

Collins, W.J., Beams, S.D., White, A.J.R., Chappell, B.W., 1982. Nature and origin of A-type granites with particular reference to southeastern Australia. Contrib. Mineral. Petrol. 80 (2), 189—200.

Collins, A.S., Pisarevsky, S.A., 2005. Amalgamating eastern Gondwana: the evolution

of the circum-Indian orogens. Earth Sci. Rev. 71, 229–270.
Cui, J.T., Bian, X.W., Wang, G.B., 2006. Geological composition and evolution of the west Kunlun. Geol. Shaanxi 24, 1–11 (in Chinese with English abstract).
Ducea, M.N., House, M.A., Kidder, S., 2003. Building the Pamirs: the view from the underside. Geology 31, 849–852.
Geng, J.Z., Li, H.K., Zhang, J., Zhang, Y.Q., 2011. Zircon Hf isotope analysis by means of LA-MC-ICP-MS. Geol. Bull. China 30, 1508–1513 (in Chinese with English abstract).
Green, T.H., 1995. Significance of Nb/Ta as an indicator of geochemical processes in the crust-mantle system. Chem. Geol. 120, 347–359.
Gibbons, A.D., Zahirovic, S., Muller, R.D., Whittaker, J.M., Yatheesh, V., 2015. A tectonic model reconciling evidence for the collisions between India, Eurasia and intra-oceanic arcs of the central-eastern Tethys. Gondwana Res. 28, 451–492.
Han, Y.G., Zhao, G.C., Cawood, P.A., Sun, M., Eizenhöfer, P.R., Hou, W.Z., Zhang, X.R., Liu, Q., 2016. Tarim and North China cratons linked to northern Gondwana through switching accretionary tectonics and collisional orogenesis. Geology 44, 95–98.
Hawkesworth, C.J., Gallagher, K., Hergt, J.M., McDermott, F., 1993. Mantle and slab contributions in arc magmas. Annu. Rev. Earth Planet Sci. 21, 175–204.
Hawkesworth, C.J., Turner, S.P., McDermott, F., Peate, D.W., van Calsteren, P., 1997. U–Th isotopes in arc magmas: implications for element transfer from the subducted crust. Science 276, 551–555.
Hofmann, A.W., 1988. Chemical differentiation of the Earth: the relationship between mantle, continental crust, and oceanic crust. Earth Planet. Sci. Lett. 90, 297–314.
Hofmann, A.W., 2003. Sampling mantle heterogeneity through oceanic basalts: isotopesand trace elementS. Treatise Geochem. 2, 61–101.
Hu, J., Wang, H., Huang, C.Y., Tong, L.X., Mu, S.L., Qiu, Z.W., 2016. Geological characteristics and age of the Dahongliutan Fe-ore deposit in the Western Kunlun orogenic belt, Xinjiang, northwestern China. J. Asian Earth Sci. 116, 1–25.
Huang, X.L., Niu, Y.L., Xu, Y.G., Chen, L.L., Yang, Q.J., 2010. Mineralogical and geochemical constraints on the petrogenesis of post-collisional potassic and ultrapotassic rocks from western Yunnan, SW China. J. Petrol. 51, 1617–1654.
Huang, H.F., Wang, J., Gao, L.Z., 2011. Oceanic and continental framework of Early Cambrian period in Tarim area. Chin. Geol. 38, 980–988 (in Chinese with English abstract).
Ji, W.H., Li, R.S., Chen, S.J., He, S.P., Zhao, Z.M., Bian, X.W., Zhu, H.P., Cui, J.G., Ren, J.G., 2011. The discovery of paleoproterozoic volcanic rocks in the Bulunkuole Group from the Tianshuihai massif in Xinjiang of northwest China and its geological significance. Sci. China (D-series) 54, 61–72.
Jiang, C.F., Yang, J.S., Feng, B.G., Zhu, Z.Z., Zhao, M., Chai, Y.C., Shi, X.D., Wang, H.D., Hu, J.Q., 1992. Opening-closing tectonics of the Kunlun mountains. In: Geol. Memoirs., vol. 5. Geological Publishing House, Beijing, p. 224 (in Chinese with English abstract).
Jiang, Y.H., Jiang, S.Y., Ling, H.F., Zhou, X.R., Rui, X.J., Yang, W.Z., 2002. Petrology and geochemistry of shoshonitic plutons from the western Kunlun orogenic belt, northwestern Xinjiang, China: implications for granitoid geneses. Lithos 63, 165–187.
Jiang, Y.H., Liao, S.Y., Yang, W.Z., Shen, W.Z., 2008. An island arc origin of plagiogranites at Oytag, western Kunlun orogen, Northwest China: SHRIMP zircon U–Pb chronology, elemental and Sr–Nd–Hf isotopic geochemistry and Paleozoic tectonic implications. Lithos 106, 323–335.
Jiang, Y.H., Jia, R.Y., Liu, Z., Liao, S.Y., Zhao, P., Zhou, Q., 2013. Origin of Middle Triassic high-K calc-alkaline granitoids and their potassic microgranular enclaves from the West Kunlun orogen, northwest China: a record of the closure of Paleo-Tethys. Lithos 156–159, 13–30.
Leake, B.E., Wooley, A.R., Arps, C.E.S., Birch, W.D., Gilbert, M.C., Grice, J.E., Hawthorne, F.C., Kato, A., Kisch, H.J., Krivovichev, V.G., Linthout, K., Laird, J., Mandarino, J.A., Maresch, W.V., Nickel, E.H., Rock, N.M.S., Schumacher, J.C., Smith, D.C., Stephenson, N.C.N., Ungaretti, L., Whittaker, E.J.W., Youzhi, G., 1997. Nomenclature of amphiboles: report of the subcommittee on amphiboles of the international mineralogical association, Commission on new minerals and mineral names. Can. Mineral. 35, 219–246.
Li, S.Z., Zhao, S.J., Liu, X., Cao, H., Yu, S., Li, X.Y., Somerville, I., Yu, S.Y., 2018. Closure of the Proto-Tethys ocean and early paleozoic amalgamation of microcontinental blocks in East Asia. Earth Sci. Rev. 186, 37–75.
Li, X.H., Li, Z.X., Wingate, M.T.D., Chung, S.L., Liu, Y., Lin, G.C., Li, W.X., 2006. Geochemistry of the 755 Ma Mundine Well dyke swarm, northwestern Australia: part of a Neoproterozoic mantle superplume beneath Rodinia? Precambrian Res. 146, 1–15.
Li, X.H., Li, W.X., Li, Z.X., 2007. On the genetic classification and tectonic implications of the early Yanshanian granitoids in the Nanling range, South China. Chin. Sci. Bull. 52 (14), 1873–1885.
Li, Z.X., Bogdanova, S.V., Collins, A.S., Davidson, A., De Waele, B., Ernst, R.E., Fitzsimons, I.C.W., Fuck, R.A., Gladkochub, D.P., Jacobs, J., Karlstrom, K.E., Lu, S., Natapov, L.M., Pease, V., Pisarevsky, S.A., Thrane, K., Vernikovsky, V., 2008. Assembly, configuration, and breakup history of Rodinia: a synthesis. Precambrian Res. 160, 179–210.
Liao, S.Y., Jiang, Y.H., Jiang, S.Y., Yang, W.Z., Jin, G.D., Zhao, P., 2010. Subducting sediment-derived arc granitoids: Evidence from the Datong pluton and its quenched enclaves in the western Kunlun orogen, northwest China. Mineral. Petrol. 100, 55–74.
Liu, Z., Jiang, Y., Jia, R., Zhao, P., Zhou, Q., 2015. Origin of Late Triassic high-K calc-alkaline granitoids and their potassic microgranular enclaves from the western Tibet Plateau, northwest China: implications for Paleo-Tethys evolution. Gondwana Res. 27, 326–341.
Ludwig, K.R., 2003. User's Manual for Isoplot 3.00: A Geochronological Toolkit for Microsoft Excel. Kenneth R. Ludwig.
Matte, P., Tapponnier, P., Arnaud, N., Bourjot, L., Avouac, J.P., Vidal, Ph, Liu, Q., Pan, Y.S., Wang, Y., 1996. Tectonics of western Tibet, between the Tarim and the indus. Earth Planet. Sci. Lett. 142, 311–330.
Mattern, F., Schneider, W., 2000. Suturing of the Proto- and paleo-Tethys Oceans in the western Kunlun (Xinjiang, China). J. Asian Earth Sci. 18, 637–650.
McCulloch, M.T., Gregory, R.T., Wasserburgm, G.J., Taylor Jr., H.P., 1981. Sm-Nd, Rb-Sr, and 18O/16O isotopic systematics in an oceanic crustal section: evidence from the Samail ophiolite. J. Geophys. Res. 86, 2721–2735.
Meert, J.G., Van der Voo, R., 1996. Paleomagnetic and 40Ar/39Ar study of the sinyai dolerite Kenya: implications for Gondwana assembly. J. Geol. 104, 131–142.
Metcalfe, I., 2011. Palaeozoic-mesozoic history of SE Asia. In: Hall, R., Cottam, M., Wilson, M. (Eds.), The SE Asian Gateway: History and Tectonics of Australia-Asia Collision, vol. 355. Geological Society of London Special Publications, pp. 7–35.
Metcalfe, I., 2013. Gondwana dispersion and Asian accretion: tectonic and palaeogeographic evolution of eastern Tethys. J. Asian Earth Sci. 66, 1–13.
Molina, J.F., Scarrow, J.H., Montero, P.G., Bea, F., 2009. High-Ti amphibole as a petrogenetic indicator of magma chemistry: evidence for mildly alkalic-hybrid melts during evolution of Variscan basic-ultrabasic magmatism of Central Iberia. Contrib. Mineral. Petrol. 158, 69–98.
Pan, Y.S., 1990. Tectonic features and evolution of the west Kunlun mountain region. Earth Sci. 3, 224–232 (in Chinese with English abstract).
Pan, Y.S., 1996. Geological Evolution of the Karakorum and Kunlun Mountains. Seismological Press, Beijing, pp. 34–78.
Pan, Y.S., Wang, Y., 1994. Discovery and evidence of the fifth suture zone of qinghai–Tibetan plateau. Acta Geophys. Sin. 37, 241–250 (in Chinese with English abstract).
Pearce, J.A., Thirlwall, M.F., Ingram, G., Murton, B.J., Arculus, R.J., Van der Laan, S.R., 1992. Isotopic evidence for the origin of boninites and related rocks drilled in the Izu-Bonin (Ogasawara) forearc, Leg 125. In: Fryer, P., Pearce, J.A., Stokking, L. (Eds.), Proceedings of the Ocean Drilling Program, vol. 125. Scientific Results, pp. 237–261.
Pérez-Soba, C., Villaseca, C., 2010. Petrogenesis of highly fractionated I-type peraluminous granites: La Pedriza pluton (Spanish Central System). Geol. Acta 8, 131–149.
Ringwood, A.E., 1974. The Petrological Evolution of Island Arc Systems [J], vol. 130. Journal of geological Society, London, 183-20.
Robinson, A.C., Yin, A., Manning, C.E., Harrison, T.M., Zhang, S.-H., Wang, X.-F., 2007. Cenozoic evolution of the eastern Pamir: implications for strain accommodation mechanisms at the western end of the Himalayan-Tibetan Orogen. GSA Bull 119, 882–896.
Robinson, A.C., Ducea, M., Lapen, T.J., 2012. Detrital zircon and isotopic constraints on the crustal architecture and tectonic evolution of the northeastern Pamir. Tectonics 31, 1–16.
Rudnick, R.L., Gao, S., 2003. Composition of the continental crust. In: Rudnick, R.L. (Ed.), The Crust, Treatise on Geochemistry, vol. 3. Elsevier-Pergamon, Oxford, UK, pp. 1–64.
Rutte, D., Ratschbacher, L., Schneider, S., Stübner, K., Stearns, M.A., Gulzar, M.A., Hacker, B.R., 2017. Building the Pamir-Tibetan Plateau—crustal stacking, extensional collapse, and lateral extrusion in the Central Pamir: 1. Geometry and kinematics. Tectonics 36 (3), 342–384.
Schwab, M., Ratschbacher, L., Siebel, W., Williams, M.M., Minaev, V., Lutkov, V., Chen, F., Stanek, K., Nelson, B., Frisch, W., Wooden, J.L., 2004. Assembly of the Pamirs: age and origin of magmatic belts from the southern Tien Shan to the southern Pamirs and their relation to Tibet. Tectonics 23, 1–31.
Suess, E., 1893. Are great ocean depths permanent? Nat. Sci. 2, 180–187.

Wolf, M.B., London, D., 1994. Apatite dissolution into peraluminous haplogranitic melts: an experimental study of solubilities and mechanisms. Geochem. Cosmochim. Acta 58 (19), 4127–4254.
Wu, F.Y., Jahn, B.M., Wilder, S.A., 2003. Highly fractionated I-type granites in NE China (I): geochronology and petrogenesis. Lithos 66 (3/4), 241–273.
Xiao, W.J., Hou, Q.L., Li, J.L., Windley, B.F., Hao, J., Fang, A.M., Zhou, H., Wang, Z.H., Chen, H.L., Zhang, G.C., Yuan, C., 2000. Tectonic faces and the archipelago-accretion process of the West Kunlun, China. Sci. China (Series D) 43, 134–143.
Xiao, W.J., Li, J.L., Hou, Q.L., Zhang, G.C., Chen, H.L., 1998. Structural style of the Southeastern West Kunlun and its implications for growing arc orogenesis. Acta Geophysica Sinica 41, 133–141.
Xiao, W.J., Windley, B.F., Hao, J., Li, J.L., 2002a. Arc-ophiolite obduction in the western Kunlun range (China): implications for the palaeozoic evolution of central Asia. J. Geol. Soc. 159, 517–528.
Xiao, W.J., Windley, B.F., Chen, H.L., Zhang, G.C., Li, J.L., 2002b. Carboniferous-Triassic subduction and accretion in the West Kunlun, China: implications for the collisional and accretionary tectonics of the northern Tibetan plateau. Geology 30, 295–298.
Xiao, W.J., Windley, B.F., Liu, D.Y., Jian, P., Liu, C.Z., Yuan, C., Sun, M., 2005. Accretionary tectonics of the western Kunlun orogen, China: a Paleozoic-Early Mesozoic, long-lived active continental margin with implications for the growth of southern Eurasia. J. Geol. 113, 687–705.
Yang, J.S., Robinson, P.T., Jiang, C.F., Xu, Z.Q., 1996. Ophiolites of the Kunlun Mountains. China and their tectonic implications. Tectonophysics 258, 215–231.
Ye, H.M., Li, X.H., Li, Z.X., Zhang, C.L., 2008. Age and origin of the high Ba-Sr granitoids from northern Qinghai-Tibet Plateau: implications for the early Paleozoic tectonic evolution of the West Kunlun orogenic belt. Gondwana Res. 13, 126–138.
Yin, A., Harrison, T.M., 2000. Geologic evolution of the himalayan Tibetan orogen. Annu. Rev. Earth Planet Sci. 28, 211–280.
Yuan, C., Sun, M., Zhou, M.F., Zhou, H., Xiao, W.J., Li, J.L., 2002. Tectonic evolution of the west Kunlun: geochronologic and geochemical constraints from Kudi granitoids. Int. Geol. Rev. 44, 653–669.
Yuan, C., Sun, M., Yang, J.S., Zhou, H., Zhou, M.F., 2004. In: Nb-depleted, Continental Rift-Related Akaz Metavolcanic Rocks (West Kunlun): Implication for the Rifting of the Tarim Craton from Gondwana, vol. 226. Geological Society, London, Special Publications, pp. 131–143.
Yuan, C., Sun, M., Zhou, M.F., Xiao, W.J., Zhou, H., 2005. Geochemistry and petrogenesis of the Yishak volcanic sequence, Kudi ophiolite, West Kunlun (NW China): implications for the magmatic evolution in a subduction zone environment. Contrib. Mineral. Petrol. 150, 195–211.
Zhang, C.L., Yu, H.F., Shen, J.L., Dong, J.G., Ye, H.M., Guo, K.Y., 2004. Zircon SHRIMP age determination of the giant-crystal gabbro and basalt in Kuda, west Kunlun: dismembering of the Kuda ophiolite. Geol. Rev. 50, 639–643 (in Chinese with English abstract).
Zhang, C.L., Yu, H.F., Ye, H.M., Wang, A.G., 2006. Aoyitake plagiogranite in western Tarim Block, NW China: age, geochemistry, petrogenesis and its tectonic implications. Science in China (Series D) 49, 1121–1134.
Zhang, C.L., Lu, S.N., Yu, H.F., Ye, H.M., 2007. Tectonic evolution of Western Orogenic belt: evidences from zircon SHRIMP and LA-ICP-MS U-Pb ages. Science in China (Series D) 50, 1–12.
Zhang, C.L., Ye, X.T., Zou, H.B., Chen, X.Y., 2016. Neoproterozoic sedimentary basin evolution in southwestern Tarim, NW China: new evidence from field observations, detrital zircon U–Pb ages and Hf isotope compositions. Precambrian Res. 280, 31–45.
Zhang, C.L., Zou, H.B., Ye, X.T., Chen, X.Y., 2018a. Tectonic evolution of the NE section of the Pamir Plateau: new evidences from field observation and zircon U-Pb geochronology. Tectonophysics 723, 27–40.
Zhang, C.L., Zou, H.B., Ye, X.T., Chen, X.Y., 2018b. A newly identified Precambrian terrane in NE Pamir: the Archean basement and Neoproterozoic granitic intrusions. Precambrian Res. 304, 73–87.
Zhang, C.L., Zou, H.B., Ye, X.T., Chen, X.Y., 2018c. Tectonic evolution of the eastern section of Western Kunlun Orogenic Belt at the northern margin of the Tibetan Plateau: new evidence from field observations and geochronology. Geosci. Front. https://doi.org/10.1016/j.gsf.2018.05.006.
Zhang, C.L., Zou, H.B., Ye, X.T., Chen, X.Y., 2018d. Timing of subduction initiation in the Proto-Tethys ocean: evidence from the cambrian gabbros from the NE Pamir Plateau. Lithos 314 (315), 40–51.
Zhang, S.B., Zheng, Y.F., 2013. Formation and evolution of Precambrian continental lithosphere in South China. Gondwana Res. 23, 1241–1260.
Zhang, S.B., He, Q., Zheng, Y.F., 2015. Geochronological and geochemical evidence for the nature of the dongling complex in south China. Precambrian Res. 256, 17–30.
Zhao, G.C., Wang, Y.J., Huang, B.C., Dong, Y.P., Li, S.Z., Zhang, G.W., Yu, S., 2018. Geological Reconstructions of the East Asian Blocks: from the Breakup of Rodinia to the Assembly of Pangea. Earth-Science Reviews In Press.
Zhu, J., Li, Q.G., Chen, X., Tang, H.S., Wang, Z.Q., Chen, Y.J., Liu, S.W., Xiao, B., Chen, J.L., 2017. Geochemistry and petrogenesis of the early Palaeozoic app0TD1.804 for